Science Advances
AAAS

advances.sciencemag.org/cgi/content/full/5/9/eaaw5519/DC1

Supplementary Materials for

Nanoscale stacking fault–assisted room temperature plasticity in flash-sintered TiO_2

Jin Li, Jaehun Cho, Jie Ding, Harry Charalambous, Sichuang Xue, Han Wang, Xin Li Phuah, Jie Jian, Xuejing Wang, Colin Ophus, Thomas Tsakalakos, R. Edwin García, Amiya K. Mukherjee, Noam Bernstein, C. Stephen Hellberg, Haiyan Wang*, Xinghang Zhang*

*Corresponding author. Email: hwang00@purdue.edu (H.W.); xzhang98@purdue.edu (X.Z.)

Published 20 September 2019, *Sci. Adv.* **5**, eaaw5519 (2019)
DOI: 10.1126/sciadv.aaw5519

The PDF file includes:

Other Supplementary Material for this manuscript includes the following:

(available at advances.sciencemag.org/cgi/content/full/5/9/eaaw5519/DC1)

Movie S1 (.mp4 format). Micropillar compression of conventional sintered TiO_2 tested at RT.
Movie S2 (.mov format). Micropillar compression of conventional sintered TiO_2 tested at 400°C.
Movie S3 (.mov format). Micropillar compression of zero-field sintered TiO_2 tested at RT.
Movie S4 (.mov format). Micropillar compression of zero-field sintered TiO_2 tested at 400°C.
Movie S5 (.mov format). Micropillar compression of flash-sintered TiO_2 tested at RT.

Movie S6 (.mov format). Micropillar compression of flash-sintered TiO_2 tested at 400°C.
Movie S7 (.mov format). Micropillar compression of flash-sintered TiO_2 tested at 200°C.
Movie S8 (.mov format). Micropillar compression of flash-sintered TiO_2 tested at 600°C.

Supplementary Materials

SUPPLEMENTARY FIGURES

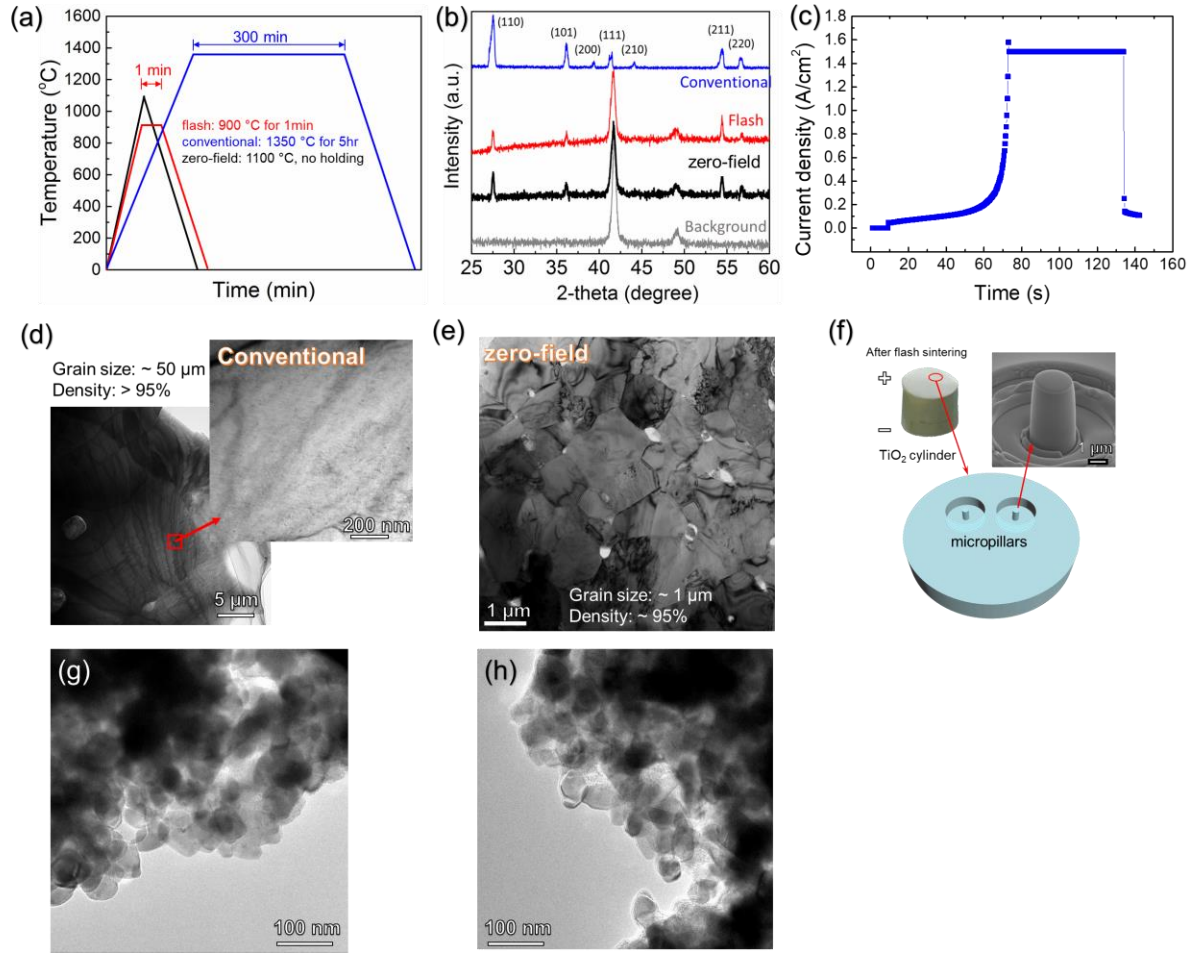

Fig. S1. Parameters for sintering of TiO_2 and the microstructures of TiO_2 prepared by various sintering techniques. (a) Sintering condition (furnace temperature vs. time) and (b) XRD profiles of flash-sintered, conventional and zero-field sintered TiO_2. Background signals in zero-field sintered and flash-sintered TiO_2 came from the sample mounting stage. Note that, the sample temperature during the onset of flash is higher than the furnace temperature. (c) Current density (A/cm^2) as a function of sintering time for flash-sintered TiO_2. (d-e) Bright-field TEM micrographs of conventional and zero-field sintered TiO_2. In both cases, the structures are relatively clean with few pre-existing defects, and similar density (95%). (f) Schematics showing micropillars fabricated on the polished surface of the sintered TiO_2 cylinder. (g-h) Bright-field TEM micrographs of nanocrystalline TiO_2 powders before flash sintering show that the as-received nanocrystalline TiO_2 powders have few defects.

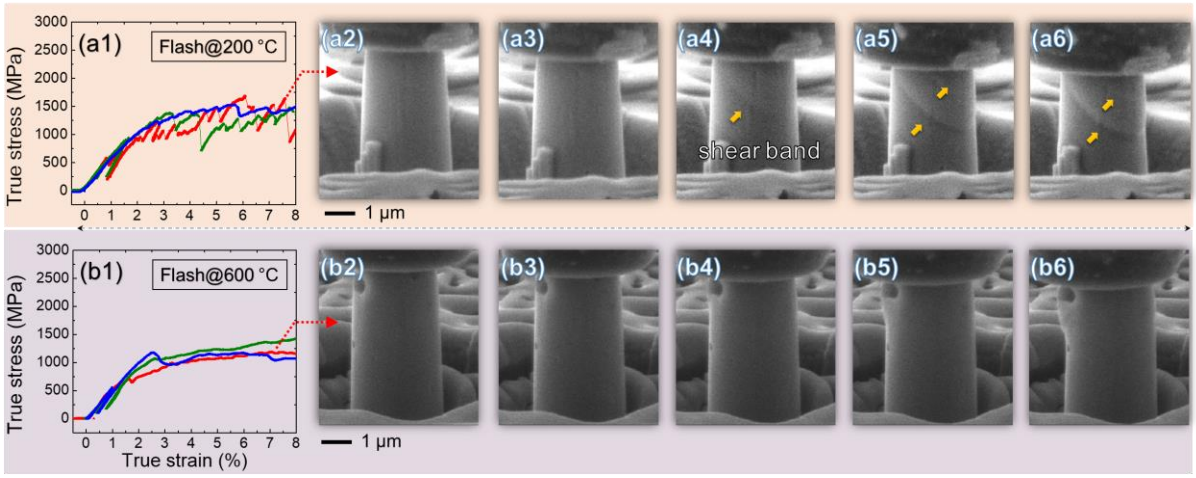

Fig. S2. True stress-strain curves and in situ movie snapshots of flash-sintered TiO_2 specimens tested at 200° and 600°C. (a1-a6) For the pillars tested at 200 ˚C, a mixture of small and large serrations was observed in the stress-strain plot. A slip band generated in the pillar broadened progressively as shown by the inserted arrows in SEM micrographs. (b1-b6) At 600 ˚C, the maximum flow stress decreases to ~ 1 GPa after a few percent of strain, and no obvious stress serrations were detected. SEM snap shots show little sign of slip bands in the deformed pillars. (See movies S7 and S8 for more details).

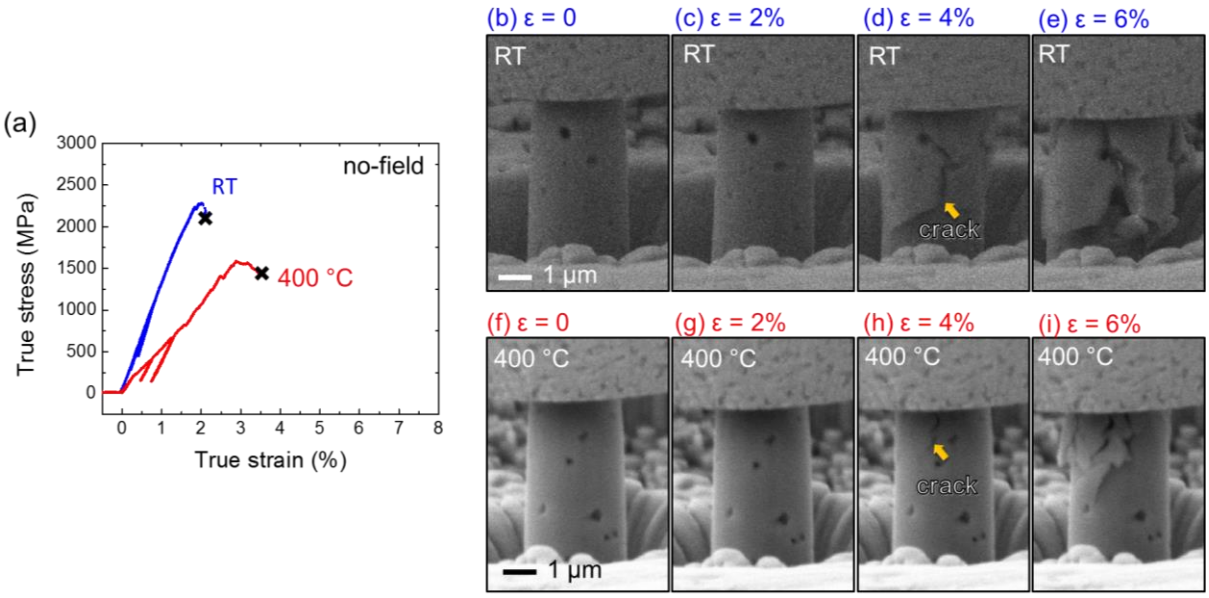

Fig. S3. True stress-strain curves and corresponding in situ movie snapshots of zero-field sintered TiO_2 tested at RT and 400°C. In both cases, the pillars experienced brittle (catastrophic) fracture at a true strain of ~ 2-3%. Partial unloading was performed to measure elastic modulus of specimens. (See movies S3 and S4 for more details).

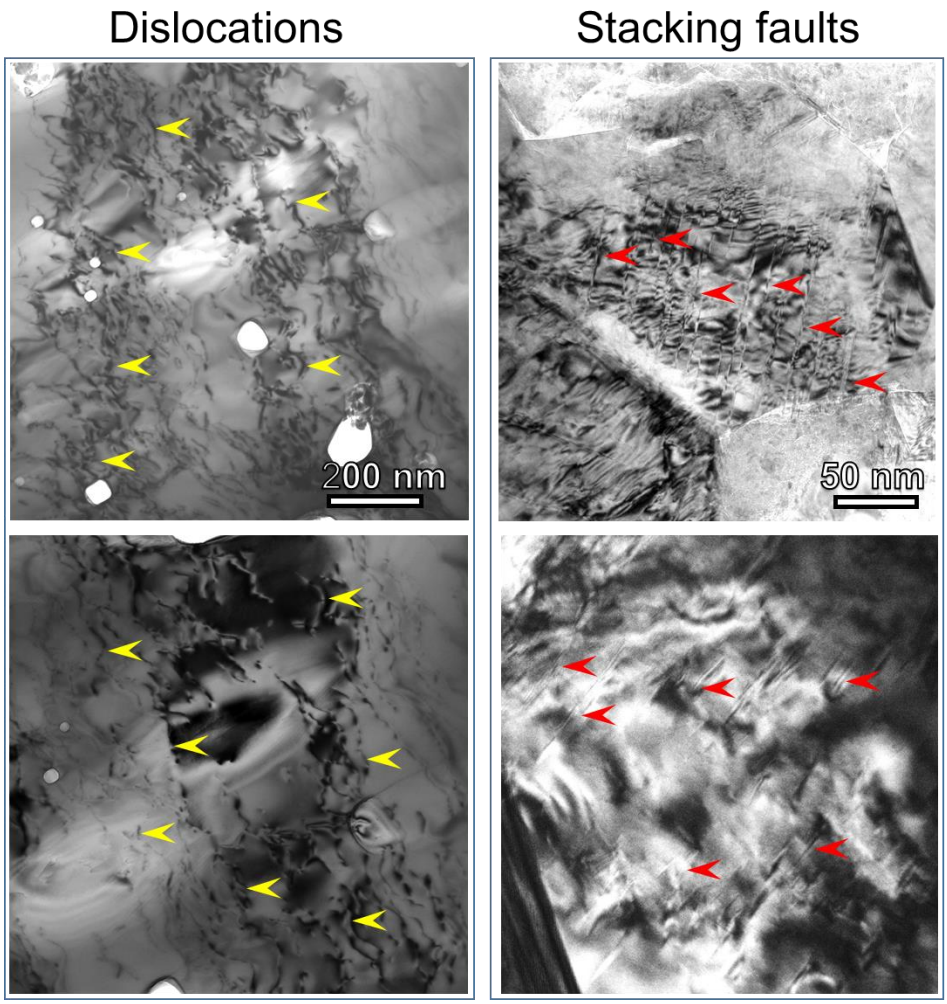

Fig. S4. Examples of abundant preexisting dislocations and stacking faults in the flash-sintered TiO_2. Yellow arrows mark dislocations; red arrows delineate stacking faults.

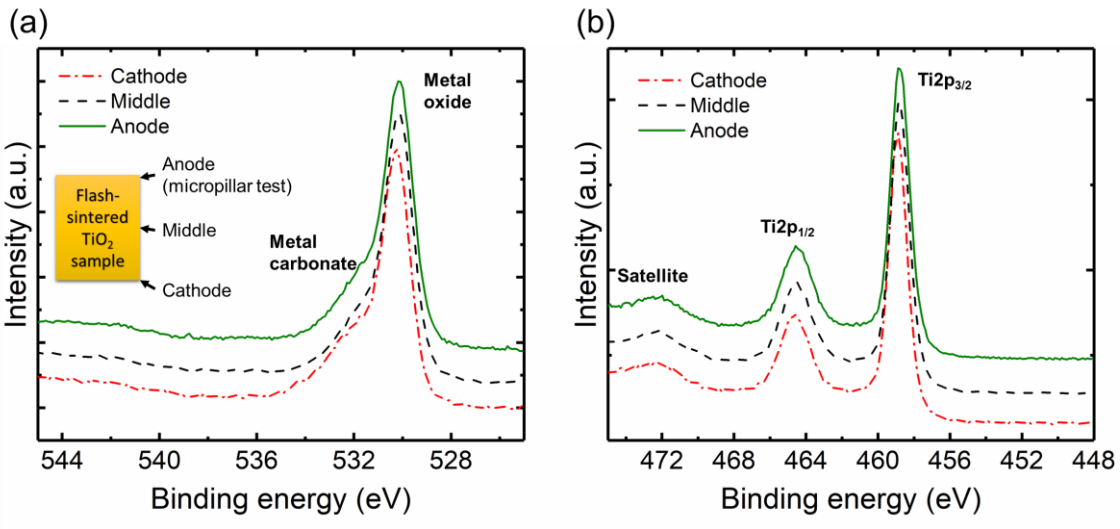

Fig. S5. XPS profiles of the flash sintered TiO_2. Normalized XPS intensity of (a) O1s peaks and (b) Ti2p peaks (background removed). Binding energies are decreased for the $Ti2p_{3/2}$ (458.9 eV to 458.7 eV), $Ti2p_{1/2}$ (464.6 eV to 464.4 eV), and O1s metal oxide bonds (530.2 eV to 530.1 eV). The small downshift, 0.2 eV, in the binding energies of the core $Ti2p_{3/2}$ and $Ti2p_{1/2}$ electrons corresponds to reduction of a portion of Ti^{4+} ions to Ti^{3+}, indicates an increased concentration of oxygen vacancies.

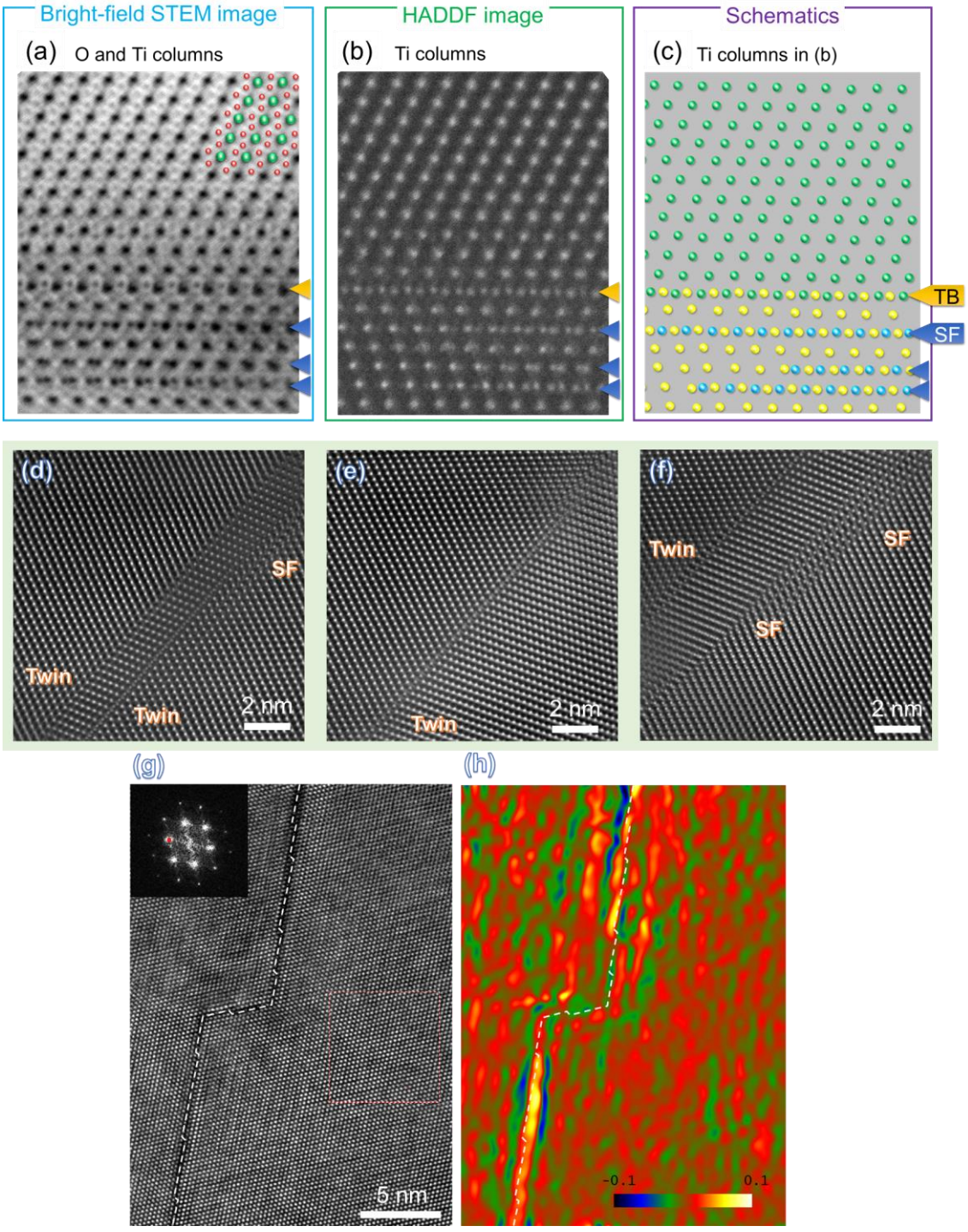

Fig. S6. High-resolution STEM micrographs of twin boundaries and stacking faults in flash-sintered TiO_2 after compression at 400°C. (a) High-resolution bright-field STEM image projected from [010] zone axis. Both Ti and O columns can be seen in the bright-field STEM image. (b) The corresponding high-angle annular dark-field (HAADF) STEM image. Only Ti columns can be resolved. (c) Schematics of Ti columns as revealed in (d). There are twice as many Ti columns along the twin boundaries and stacking faults as compared to the perfect

crystal lattices. Ti columns are shown in different colors for clarity. (d-f) More examples show that the number of Ti columns along the twin boundaries and stacking faults increases as compared to the perfect crystal lattice. (g-h) Geometric phase analysis (GPA) of stacking faults inside the flash sintered TiO_2. (g) An original HRTEM image. (h) The corresponding stress map showing tensile stress (light-yellow color) along the stacking fault, and compressive stress (dark blue color) adjacent to the stacking faults.

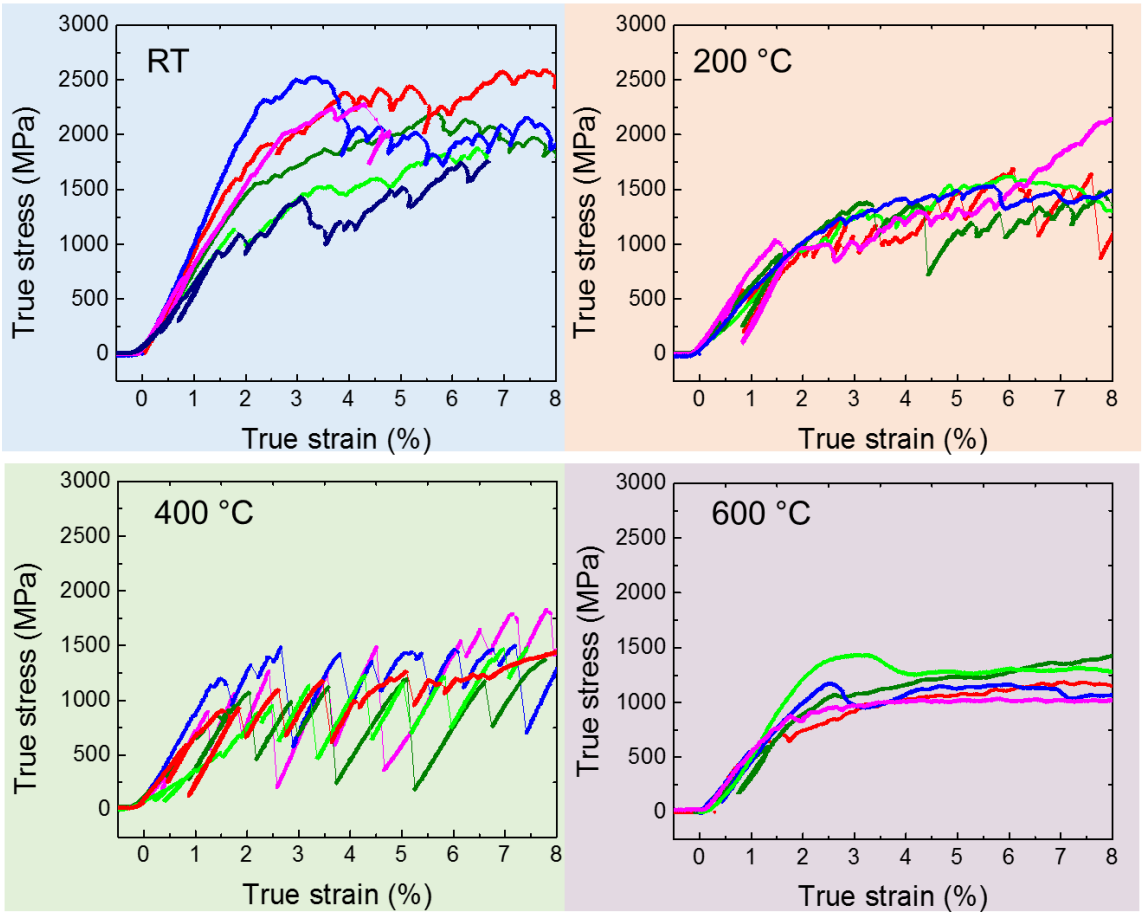

Fig. S7. Stress-strain curves of flash-sintered TiO_2 obtained from in situ micropillar compression tests at different temperatures. At each temperature, multiple (at least 5) compression tests have been performed.

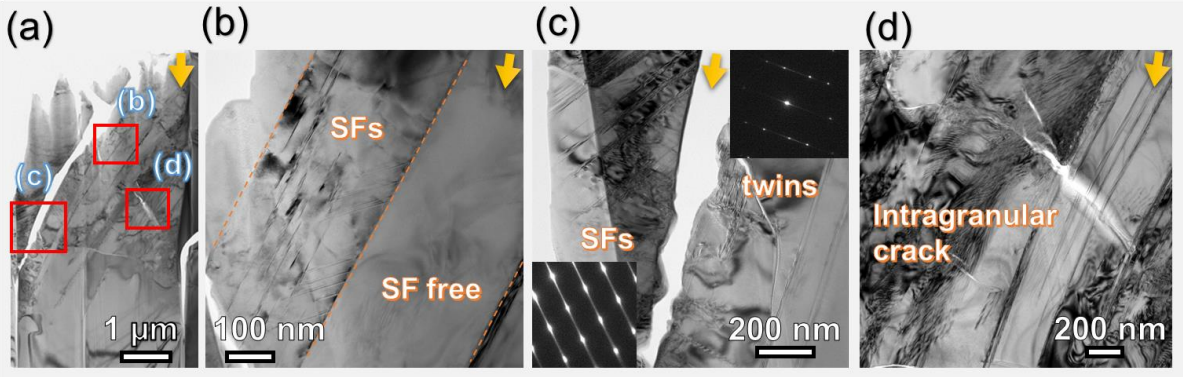

Fig. S8. Bright-field TEM micrographs of a compressed conventional sintered TiO_2 pillar tested at RT. (a) Low-magnification TEM image of the compressed pillar. A small top portion of the pillar is damaged (removed) during FIB milling. (b-c) Scattered stacking faults and twin boundaries formed after compression. However, the density of stacking faults and twin boundaries is much lower as compared to the deformed flash-sintered TiO_2 at RT. (d) The formation of intragranular cracks after compression. Such cracks were not observed in deformed flash-sintered TiO_2.

SUPPLEMENTARY METHODS

XPS analyses

The chemistry of flash-sintered TiO_2 specimen has been analyzed using ThermoFisher K-Alpha X-Ray Photoelectron Spectroscopy (XPS) with 1486.7 keV x-ray photon energy and 400 μm spot size. Three positions corresponding to the anode side, middle and the cathode side have been analyzed as shown in the embedded image in Fig. R2 (a). A downshift of the binding energies for the $Ti2p_{3/2}$ (458.9 eV to 458.7 eV), $Ti2p_{1/2}$ (464.6 eV to 464.4 eV), and O1s metal oxide bonds (530.2 eV to 530.1 eV) has been observed. The small downshift, 0.2 eV, in the binding energies of the core $Ti2p_{3/2}$ and $Ti2p_{1/2}$ electrons corresponds to reduction of a portion of Ti^{4+} ions to Ti^{3+}, indicates an increased concentration of oxygen vacancies.

Movie S1. Micropillar compression of conventional sintered TiO_2 tested at RT.

Movie S2. Micropillar compression of conventional sintered TiO_2 tested at 400°C.

Movie S3. Micropillar compression of zero-field sintered TiO_2 tested at RT.

Movie S4. Micropillar compression of zero-field sintered TiO_2 tested at 400°C.

Movie S5. Micropillar compression of flash-sintered TiO_2 tested at RT.

Movie S6. Micropillar compression of flash-sintered TiO_2 tested at 400°C.

Movie S7. Micropillar compression of flash-sintered TiO_2 tested at 200°C.

Movie S8. Micropillar compression of flash-sintered TiO_2 tested at 600°C.